Experimental investigation of tsunami bore impact force and pressure on a square prism

Seyedreza Shafiei *, Bruce W. Melville, Asaad Y. Shamseldin

The University of Auckland, Department of Civil and Environmental Engineering, Auckland, New Zealand

ABSTRACT

The 2004 Indian Ocean tsunami and the recent 2011 Japan tsunami have highlighted the need to investigate the interaction between tsunamis and coastal structures. Although some efforts have been made to determine tsunami loads on structures, there are discrepancies between the limited number of published design guidelines. This study comprises an experimental investigation of a tsunami bore interaction with an inland structure. Physical modelling of the tsunami bore in the laboratory allowed study of the impact of tsunami bores on a square prism model having different orientations to the flow direction. The use of common geometrical shapes simplifies experiments and increases the reliability of results. The experiments were conducted in a 14 m long, 1.2 m wide and 0.8 m deep wave flume equipped with an automatic gate designed to generate a tsunami bore. Measurements were made of the forces and pressures exerted on the model structure and of the bore heights and velocities. The vertical pressure distribution was measured on what was initially the structure's front wall, with the front wall at 0°, 30°, 45°, 60°, 90° and 135° to its original alignment. A relation between bore velocity and bore height is presented. The measured maximum forces in the stream-wise and upward directions were numerically modelled successfully, and relevant drag coefficients were determined for the structure at different orientations.

© 2015 Elsevier B.V. All rights reserved.

1. Introduction

Tsunamis are large ocean waves that are caused by a variety of natural phenomena such as earthquakes, landslides (sub-areal and submarine), volcanic eruptions and comets. Their effects on coastal communities are often catastrophic, as recently demonstrated by the 2004 Indian Ocean and 2011 Japan tsunamis.

Severe damage or collapse of structures and large loss of human life from the 2004 Indian Ocean tsunami illustrate the destructive nature of tsunamis (Fritz et al., 2006; Ghobarah et al., 2006; Saatcioglu et al., 2006; Tomita et al., 2006). More recently, the 2011 Japan tsunami killed thousands of people and destroyed coastal infrastructure (Foytong et al., 2013; Fritz et al., 2012; Liu et al., 2013; Shimozono et al., 2012). These recent tsunami events highlight the need to advance investigation of the interaction between tsunamis and coastal structures. Coastal areas in the seismically active Pacific Rim are experiencing rapid development of residential and tourist infrastructure, resulting in a significant increase in the number of coastal structures at risk of tsunami damage. As a consequence, better understanding of tsunami interaction with coastal structures is vital.

Depending on location and tsunami characteristics, some tsunamis break off shore and transform into a tsunami bore (Yeh, 1991). A bore is a broken wave with uniform depth and infinite wavelength, characterized by a turbulent but relatively gently sloping wave front (Hibberd and Peregrine, 1979). As the tsunami bore approaches the shoreline, the water velocity approaches the wave propagation velocity, resulting in an accumulation of turbulence at the front of the bore. Yeh (1991) proposed that this turbulence is increased by a momentum exchange between the bore and a small wedge of initially still water in front of the bore. The energy of this high turbulence is released on the dry shore and can cause extensive damage (Yeh, 1991). Kihara et al. (2015) proposed that the main body of the flow profile can be described using the ideal flow model of Ritter (1892), but in the leading edge or tip region of the bore flow resistance is important and the profile in this region is better described by a real fluid model (e.g. Chanson (2006)).

The inland tsunami flow depth and velocity are highly variable. During the 2004 Indian Ocean tsunami, the flow depth at the southern part of Khao Lak reached between 4 and 7 m (Dias et al., 2006; Matsutomi et al., 2006). The tsunami flow velocities were estimated at between 3 and 4 m/s at Kumala beach and 6 to 8 m/s at Khao Lak (Rossetto et al., 2007). Tsunami flow velocities have been calculated to be as high as 8 m/s, or estimated at up to 16 m/s (Ramsden, 1993). For the 2011 Japan tsunami, reported maximum flow depths were 8 m at Kamaishi City (Fraser et al., 2012), and 6 m at Arahama Town (Suppasri et al.,

* Corresponding author at: The University of Auckland, Auckland, New Zealand. Tel.: +64 2102996547.
  E-mail address: ssha399@aucklanduni.ac.nz (S. Shafiei).

2012). In Sendai, the tsunami flow velocities reached approximately 8 m/s at about 1 km inland of the shoreline (Hayashi and Koshimura, 2013). In another area close to the Sendai Airport, the tsunami flow velocity was about 10 to 13 m/s (Jaffe et al., 2012).

The flow generated from rapid release of water from a sluice gate or a radial gate is similar to a tsunami bore (Chanson, 2006; Cross, 1967; Yeh, 2006), and has been adopted in tsunami–structure interaction studies by various researchers (Arnason, 2005; Nistor et al., 2011; Nouri, 2008; Rahman et al., 2014). Accordingly, in the present study, a tsunami bore was simulated by the almost instantaneous opening of a sluice gate which impounded a large volume of water.

Many experiments have been carried out in laboratory flumes to investigate tsunami bore impact on (a) a vertical wall blocking the flume width (Cross, 1967; Kihara et al., 2015; Linton et al., 2013; Mizutani and Imamura, 2001; Robertson et al., 2011; Robertson et al., 2013; Santo and Robertson, 2010), and (b) low rise coastal structures with wave overtopping (Asakura et al., 2000; Iizuka and Matsutom, 2000; Rahman et al., 2014; Thusyanthan and Madabhushi, 2008). However, the interaction between a tsunami bore and a three dimensional structure where the flow does not overtop the structure has received limited attention because of the complexity of tsunami bore flow around such a structure (Wijatmiko and Murakami, 2012). Research that has been carried out has been restricted to the investigation of tsunami bore impact on the front wall (perpendicular to the flow) and side wall (parallel to the flow) (Chinnarasri et al., 2013; Fujima et al., 2009; Nouri et al., 2010; Palermo et al., 2012; Palermo et al., 2009; Robertson et al., 2008).

Previous studies have produced both similar and contradictory results for the tsunami induced pressure. For example, Nouri et al. (2010) investigated the pressure distribution on the front wall and side wall of a square prism structure due to a tsunami bore. Their study identified two types of exerted pressure: (a) an impulsive pressure with a short duration (order of milliseconds) and (b) a quasi-steady pressure with a longer duration than impulsive (order of seconds). Recently, Kihara et al. (2015) studied the impact of a tsunami bore on a vertical wall and similar observations for the impulsive pressure phase similar to that of Nouri et al. (2010). However, Nouri et al. and Kihara et al. have dissimilar observations for the quasi-steady phase pressure as compared with the hydrostatic pressure at the bore height. Nouri et al. (2010) reported quasi-steady phase pressures greater than hydrostatic pressure while Kihara et al. (2015) reported pressures almost equal to the hydrostatic pressure.

The following types of tsunami forces have been identified by researchers: (a) horizontal forces, including impulsive, hydrostatic, and hydrodynamic forces; and (b) vertical forces, including impulsive, hydrodynamic drag, hydrodynamic lift, and buoyant forces (Yeh, 2007). Cross (1967) investigated tsunami bore propagation in a flume and measured the bore-induced stream-wise force on a vertical wall. Cross found that, for the case of uniform steady flow impinging on a vertical wall and for a bore front slope of less than 15°, the total stream-wise force is the summation of a hydrostatic force and a hydrodynamic force. This statement of Cross (1967) is used as a basis in this study for evaluating the bore force on a rectangular prism structure. The previously cited have provided useful information for designing coastal structures (e.g. seawalls and buildings) in tsunami prone regions. The results and findings have contributed to the preparation of tsunami design guidelines.

Specific tsunami design guidelines for coastal structures have been prepared by authorities in the United State of America (USA). The City and County of Honolulu (CCH) specified equations for estimation of the forces affecting buildings due to coastal flooding, including hydrostatic, hydrodynamic (drag), surge and buoyant forces (CCH, 2000). The Federal Emergency Management Agency (FEMA) stated that tsunami loadings may be treated in the same way as wave loading and flood loading but on a much larger scale (FEMA, 2011). However, in guidance for design of tsunami vertical evacuation shelters, FEMA states that

there are significant differences between a tsunami and flooding or storm surge (FEMA, 2012). Amongst these guidelines, there are significant differences amongst the estimates of tsunami force on the structures. In spite of the guidance outlined above, there are significant shortcomings in the field of tsunami design. For example, until the recent Japan 2011 tsunami, it was assumed that reinforced concrete structures would withstand tsunamis. However, during the Japan tsunami many reinforced concrete structures collapsed because of the unexpected magnitude of tsunami loads (Yeh et al., 2013).

Lloyd and Rossetto (2012) and Cawley (2014) reviewed the existing design guidelines and found that the guidelines have not used unified notation for characterising tsunami waves, and have not addressed the load combinations consistently. Cawley (2014) stated that most guidelines have addressed tsunami forces based on their own experimental results. Consequently, Cawley (2014) emphasised the need for further investigation of the effect of building shape and orientation in estimating tsunami loadings, and for definition of the flow depth and velocity.

Measurements of the action of a tsunami bore on a square prism structure at different orientations to the flow direction are presented. The bore height and velocity were measured in the flume upstream the structure, and an empirical relationship between the bore height and velocity was derived; the empirical relationship was compared with those from previous studies. To study the effect of structure orientation on the bore induced pressure, the vertical distribution of the pressure on the front wall of the structure was measured at 0°, 30°, 45°, 60°, 90° and 135° to the flow direction. In most of the previous studies, pressures were measured at only 0° and 90°. In addition, the bore induced stream-wise and upward forces, and moments, were measured at the base of the structure. The findings by Cross (1967) were used to compute the stream-wise force theoretically, and the theoretical calculation was validated using the experimental results. The additional orientations allow drag coefficients to be proposed for all orientations of a square prism structure. The upward force on the structure due to the bore impact was theoretically computed assuming the total upward force being due to the buoyancy, and the results were validated using the experimental data. Concurrent measurement of force allowed evaluation of the pressure measurement technique and of the integration of the pressures to give a total force.

2. Experimental set-up

2.1. Facility

A 14 m long, 1.2 m wide and 0.8 m deep wave flume, connected to a reservoir 11 m long, 7.3 m wide and 0.6 m deep, was used (Fig. 1). The flume is equipped with an automatic gate to generate a tsunami bore. The flume has concrete block side walls and a horizontal bottom of moderately smooth concrete to enable simulation of tsunami bore propagation over a plane dry bed. The flume is emptied using the drain gate and drain channel.

The 1.20 m wide and 0.9 m high automatic gate consists of a sliding gate and a shutter gate, both of which open rapidly, providing near-instantaneous water release (Fig. 2). The vertical-rise sliding gate controls water release, while the shutter gate ensures uniform flow distribution across the flume. The sliding gate opening is automatic; it is timed to remain open for 4 seconds before automatically closing. The sliding gate is rapidly lifted by a hydraulic piston actuated through a computer program. The shutter gate opening is also automatic. It is almost instantaneously opened by a pneumatic cylinder; after manual initiation of opening on an electronic signal from the opening of the sliding gate it is also timed to remain open for 4 s before automatically closing. The simultaneous operation of the two gates facilitates the generation of a stable bore with a reasonably smooth water surface. In addition, the combination of the gate and shutter minimises any leakage of water into the flume before gate opening. The sliding gate opening height is
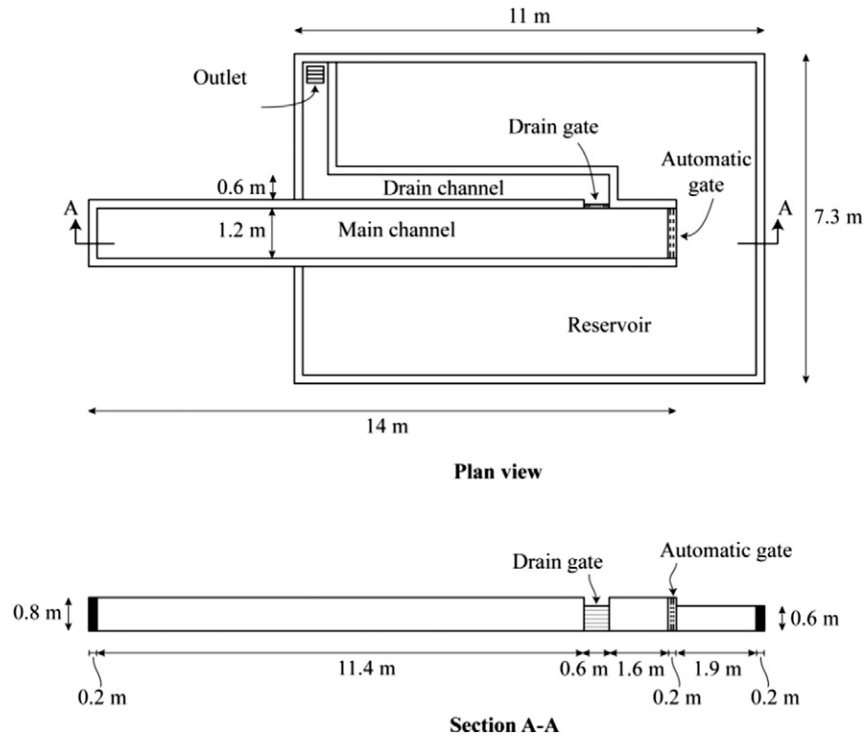
Fig. 1. Experimental set-up: plan view of the flume and its attached reservoir, and side section of the flume.

adjustable; this, combined with variation in water depth in the reservoir, enables generation of different bore heights and velocities.

2.2. Instrumentation

Five capacitance-type wave gauges were placed 20 mm above the flume floor at the centre of the flume along its length, to measure the depth of flow and allow observation of the formation and propagation of the bore. The precision of the wave gauges used in the experiments is 2 mm. The first wave gauge (Wave gauge 1) was placed 2.5 m downstream from the gate, with the remaining gauges (numbered Wave gauge 2 to Wave gauge 5) equally spaced 1.75 m apart over a total distance of 9.5 m downstream from the gate. The approaching

Fig. 2. Details of gate. Photo is looking towards the gate from 2 m downstream of the gate.

bore featured a sloping front, as is typical for such experiments. The measured bore height used herein is the maximum water depth measured by the wave gauges behind the sloping front of the approaching bore (see Fig. 6). The average bore velocity was calculated using the recorded time at which the bore struck each wave gauge. This was taken to be the time of the first non-zero reading at the wave gauge. The wave gauges were logged at 1 kHz.

The $300 \times 300 \times 600$ mm square-prism model structure ('the structure') was constructed from acrylic sheets, 5 mm thick for the walls and 10 mm thick for the base. The structure was placed 10 m from the gate (i.e. 500 mm beyond the final wave gauge). To measure the pressure on the model structure surface, five differential pressure sensors (Honeywell 26PC series) were placed inside the structure and attached along the height of the model structure, with the first one (Sensor 1) placed 32 mm above the base of the structure (Fig. 3b). The other four pressure sensors (numbered Sensor 2 to Sensor 5 with the latter being the highest) were evenly placed at 42 mm intervals above the first sensor, i.e. over an overall height of 200 mm above the base. The reference pressure for the differential pressure sensors was a tank of water with water level 50 mm above the base of the structure. Two different pressure sensor capacities were used in the experiments. Sensors 1 and 2, at the lower part of the structure (which were exposed to larger pressure) had 34.47 kPa capacity with precision of ± 0.043 kPa and response time of 1 ms. The remaining sensors higher up the structure (which were exposed to smaller pressure) had 6.89 kPa capacity with precision of ± 0.0086 kPa and response time of 1 ms. Also, the latter low capacity pressure sensors were used to measure the bore induced pressure on the structure with orientations greater than 0°. Each pressure sensor was fitted with two flexible transparent rubber tubes and the pressure difference between these tubes was measured (Fig. 3b). One of the tubes was exposed to the reference pressure, while the second tube was mounted flush with the surface of the structure. Both tubes were filled with water and were checked for air bubble removal before each experiment.

The top of the structure was sealed with a sheet of acrylic with a 60 mm diameter tube extending 300 mm from the top. The connections for the pressure sensors were fed through this tube to protect the
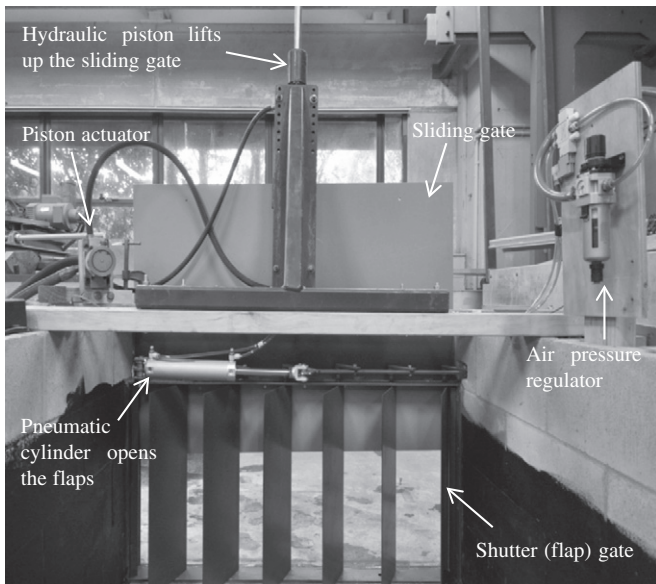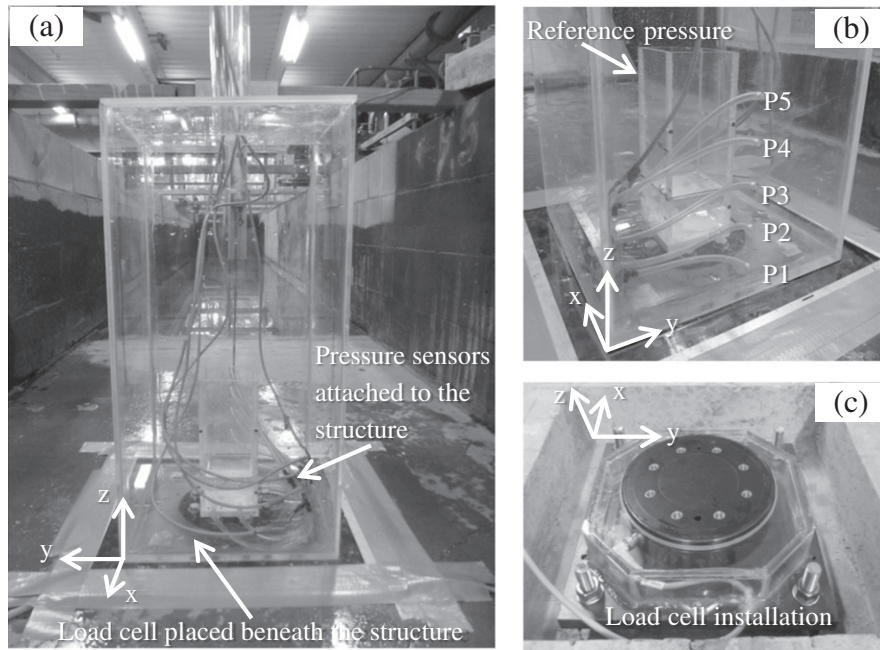
Fig. 3. Pressure sensors and load cell installation: (a) structure placed 10 m downstream of the gate (photo is looking towards the gate; (b) pressure sensor locations on the front wall of the structure at $\theta = 0°$; (c) load cell fixed in the recess, looking in the flow direction.

pressure sensors from water damage. The structure was made without openings so that the maximum force and pressure was applied to the structure. In real buildings, the forces would probably be attenuated, with the main attenuation factors being due to openings, broken walls, and wall deformation.

A JR3 multi-axis waterproof load cell, model 75E20A4, was used to measure force and moment acting on the structure in three dimensions with the positive x-axis aligned with the flow direction (Fig. 3c). The full scale ranges of force measurements are 2 kN, 2 kN and 4 kN in the x, y and z directions, respectively, and the full scale range of moment measurement was 0.4 kN m in each direction. The precision of the load cell in each axial direction is 0.005 N and 0.001 N m for force and moment measurements, respectively. The load cell was mounted in a recess below the flume floor to allow the base of the model structure to be level with the floor of the flume. The load cell was calibrated by the manufacturer and a 6 by 6 calibration matrix was provided to convert the output signals to force and moment values. The sampling rate of data collection for the load cell and pressure sensors was 1 kHz.

A high speed video camera (Casio EX-FH100) was used to film the bore impact on the structure at different orientations, with floodlighting to improve the video quality. The camera was operated at 240 frame per second (fps).

2.3. Experimental procedure

For the experiments, the reservoir was filled to a depth of 400 mm, 500 mm or 600 mm, and the sliding gate was lifted to a constant height of either 200 mm or 300 mm. Table 1 lists six different combinations of gate opening height (GO) and reservoir water depth (WL) which were

Table 1
Different cases of the bore height and velocity combinations.

Case	WL (mm)	GO (mm)	h_b (mm)	u_b (m/s)
Case 1	400	200	140	1.98
Case 2	400	300	150	2.08
Case 3	500	200	160	2.14
Case 4	500	300	170	2.2
Case 5	600	200	190	2.33
Case 6	600	300	210	2.45

used to obtain six experimental cases with different bore heights (h_b) and velocities (u_b). For each case, the bore height and the bore velocity were taken as the mean values from five repetitions.

The maximum volume of water stored in the reservoir is between 26 and 39 m^3, depending on the depth of water in the reservoir. The volume released during an experiment is from 1 to 3 m^3, depending on the water depth in the reservoir and gate opening height. The released volume is less than 10% of the reservoir volume, and it is assumed that the small drop in water head in the reservoir does not affect bore height or velocity during an experiment.

The sliding gate opening system used in this study (computer-controlled hydraulic piston) allowed a gate-rising speed of 0.65 m/s to be achieved. For this gate rising speed, the lifting time of the gate (t_{lif}) was calculated as 0.31 s and 0.46 s for the 200 mm and 300 mm gate opening heights (GO), respectively. The time for GO = 300 mm exceeds the Lauber and Hager (1998) consideration for instantaneous dam break ($t_{lif} = (2 \times WL / g_n)^{0.5} = 0.29$ s, for WL = 400 mm). However, as shown in the Results and discussion section, the bore front profile is close to that of the analytical solution by Chanson (2006.)

The stream-wise force (F_x) and the upward force (F_z) are expected to change as a function of the bore height, bore velocity, and orientation of the structure. Thirty six experiments were undertaken comprising different combinations of reservoir water depth, gate opening and structure orientation. The structure was initially oriented with the front wall at right angles to the incoming bore (0°) and subsequently rotated through 30°, 45°, 60°, 90° and 135° to its original alignment (Fig. 4). Fig. 4 also shows the positions of the pressure sensors attached to the structure and the projected widths of the structure to the oncoming bore. For each of the 36 experiments, five repetitions were made to ensure consistency of the results, giving a total of 180 tests.

3. Results and discussion

Froude scale modeling was used to convert model measurements to prototype quantities. Geometrical similarity was based on an assumption that the maximum average bore height generated in this study is equivalent to 5 m flow depth (inundation depth) during a real tsunami. This assumption is based on field measurements of flow depth of
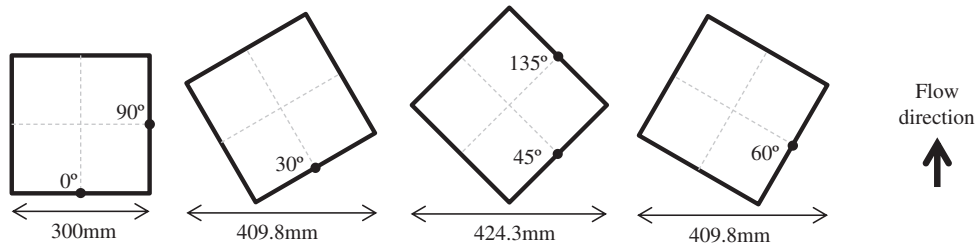
Fig. 4. Structure orientations with respect to the original alignment of the front wall, pressure measurement points (solid circles), and projected widths of the structure.

previous tsunami events as described earlier. The assumption resulted in a geometrical similarity scale of 1:25 for this study.

3.1. Bore characteristics

Multiple bores were produced and the bore height time history was measured at each wave gauge along the flume, as shown in Fig. 5 for Case 6. The coefficient of variation of the measured bore height for each gauge was less than 5% over the five repetitions of an experiment (Fig. 5a), confirming the repeatability of the system of generating model bores. The times of bore arrival at a gauge, and hence the bore velocity measurements, also showed a variation of less than 5% for each experiment, again confirming consistency of the method of bore generation.

The generated bore took about 4 s to travel the 10 m length of the flume to reach the structure, with bore velocities in individual experiments ranging from 1.98 to 2.45 m/s, corresponding to prototype velocities ranging from 9.9 to 12.25 m/s. The initial rapid rise of bore height at each gauge records the passing of the sloping bore front. Because the tsunami bore generated in this study is similar to a dam-break flow (Chanson, 2006), the bore front profile from this study was compared with the profile from analytical solutions of Ritter (1892) and Chanson (2006) for dam-break flow. To obtain the bore front profile, the average measured velocity was used to transform the initial rapid-rise part of the bore height in the time-domain (the time history in Fig. 5) to the bore height in the distance-domain (the bore front profile in Fig. 6).

For example, for Case 6, Fig. 6 shows the height of the bore front over a distance of 2 m from its leading edge. The resulting bore front profile is what would be recorded in a photograph of the leading 2 m of the front of the bore, taken from the side of the flume. The obtained bore front profile is similar to that obtained from analytical solution proposed by Chanson (2006). The experimental results from this study show that Ritter's solution is not valid for the bore front profile, because experimental measurements show that the front of the generated bore has a sloping, slightly-rounded, convex-up profile.

A number of equations have been proposed to calculate the bore propagation velocity from the measured bore height (h_b), including those by Murty (1977); Kirkoz (1983); Bryant (2001); FEMA (2012), and Matsutomi and Okamoto (2010), all with the form

$$u_b = \alpha_u (g_n h_b)^{0.5} \tag{1}$$

where α_u is a constant and g_n is the gravitational acceleration. The equations are compared in Fig. 7, which indicates significant variation amongst the equations.

The results from this study are also plotted in Fig. 7. For an equation with the form of Eq. (1), the least squares fit to the results gives an α_u value of 1.7. The resulting predicted velocities are within 7% and 15% of those predicted by the equations of Murty (1977) and FEMA (2012), respectively.
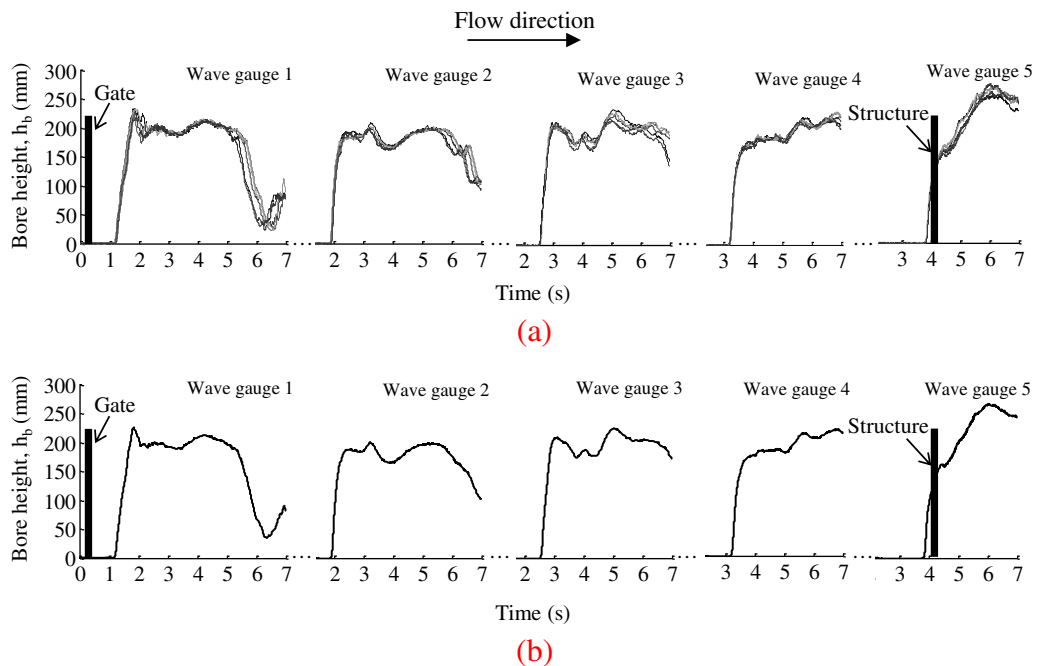

Fig. 5. Time histories of (a) five repetitions and (b) average measured bore height, for each wave gauge along the length of the flume. Note positions of gate, wave gauges and structure on x axis.
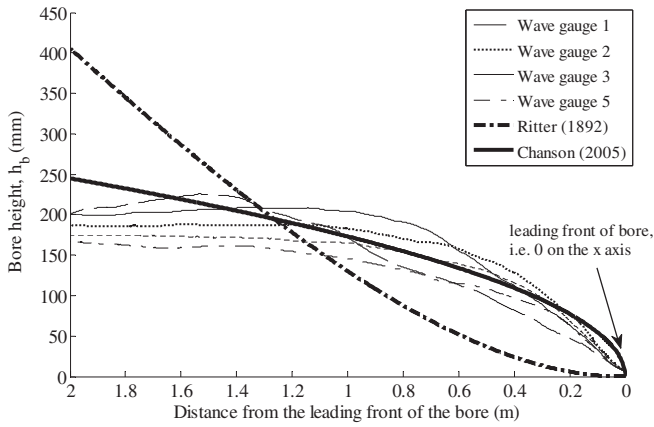
Fig. 6. Bore front profile at different wave gauge locations for a 2 m length of the bore with respect to its leading front. Note 0 on the *x* axis indicates the leading front of the bore.

3.2. Vertical distribution of tsunami-induced pressure on the model structure

Fig. 8 shows photographs (taken from downstream and extracted from video records) of the generated bore approaching the structure. Fig. 6 and the photographs show the sloping front of the bore, which was observed to have a maximum angle of about 15° to the horizontal. A small amount of air entrainment was observed in the bore front but not in the water behind the front. The initial bore impact force might be slightly influenced by this air entrainment.

For the experiments where the front wall of the structure was perpendicular to the flow direction (i.e. at $\theta = 0°$), Figs. 9 and 10 show photographs taken during bore impingement and the average pressure (averaged over five repetitions) profiles at different sensor locations. The pressure sensors mounted near the bottom of the structure (Sensors 1 and 2) were exposed to an impulsive pressure resulting from the sloping front of the bore profile (Cooker and Peregrine, 1995; Hattori et al., 1994; Okamura, 1993), while Sensors 3, 4 and 5 did not initially experience the impulsive pressure (Fig. 10). But immediately after the initial bore impact, the water level increased in front of the structure and covered the other three sensors. This lag in sensor response is a consequence of the sloping front of the bore. Pressure measurements were discontinued 3 s after the initial bore impact when backflow of water disturbed the experiments (Fig. 10). In Fig. 10, $t = 0.0$ s is the time of gate opening. This zero time applies to all figures except those illustrating pressure distribution analyses (Figs. 12 to 15). However, to obtain average time histories of pressures,
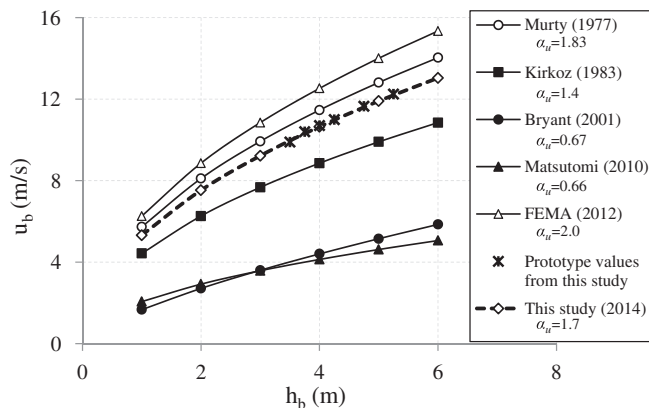
the time histories from individual repetitions were synchronised by shifting them small amounts sideways (i.e. along the time axis) so that the initial positive impulsive pressures all occurred at $t = 4.0$ s. This method of synchronisation was applied to all the figures containing time history in this study. As discussed later in this section, however, for the pressure distribution analyses in this study (Figs. 12 to 15), $t = 0.0$ s is the time of the initial impact of the bore on the structure (i.e. the time at which sensors started to measure the exerted pressure).

Typically, the pressure curves can be separated into two main phases. The first phase is the impulsive part, where high values are reached for a short time (of the order of milliseconds) and is associated with the initial impact of the bore. The second phase is a longer quasi-steady state with lower values over a longer time (of the order of seconds). The pressure fluctuations in the second phase are probably due to variations in the amount of air trapped between the bore and the structure, or vibration of the structure, while the bore is flowing past the structure (Nouri et al., 2010). In producing Fig. 10, the measured pressure time histories from each repetition were synchronised so that the initial impulsive pressures from all the repeats coincide with each other. Subsequently, the average pressure profile from five repetitions was created.

Case 6 was used as an example because it resulted in the maximum pressures. From Fig. 10, it is apparent that Sensor 1 recorded a higher impulsive pressure than that of Sensor 2. This is consistent with the observations of Robertson et al. (2008), Nouri et al. (2010) and Al-Faesly et al. (2012). The average maximum impulsive pressure was recorded to be about 9 kPa in these experiments, which is in agreement with the pressure measured by Robertson et al. (2008), who used a large scale experimental set-up. However, the structure used by Robertson et al. was a vertical wall, blocking the flume width, where the bore did not flow around the vertical wall.

Examples of the five repetitions of the measured pressures for Sensors 1 and 2 are shown in Fig. 11. The graphs demonstrate the repeatability of the experiments.

Both Sensors 1 and 2 experienced a sudden reduction of the impulsive pressure magnitude to the quasi-steady pressure (Fig. 11). This reduction was up to 50% of the maximum impulsive pressure observed at Sensors 1 and 2, which is also consistent with previous studies (Nistor et al., 2011; Nouri et al., 2010). It was also observed that the magnitude of the impulsive pressure was not always repeatable, and it was more random for stronger bores. However, the profile of the applied pressure was consistent. The results of other studies suggest that the magnitude of the impulsive pressure is a maximum when there is a very small amount of air trapped between the wall and the wave; if a larger amount of air is trapped, the magnitude is lower (Bullock et al., 2007; Hattori et al., 1994; Kirkoz, 1983; Peregrine, 2003). In the present experiments the small amount of air trapped was subjected to random variations caused by the bore turbulence. In addition, in some experiments, after the initial bore impact the pressure dropped to below zero. This may be a consequence of pressure transients (water-hammer effect) in the water inside the plastic tubes used for connection between the pressure sensors and the structure. The effect was attenuated immediately after the initial impact of the bore.

Fig. 12 shows, for Case 6, the normalised maximum pressure at Sensor 1 for the different structure orientations, at the time of impact ($t = 0$) and for various times after impact. Note that for all pressure distribution analyses, for each structure orientation, $t = 0$ is defined as the time when the bore front reached the alignment of the pressure sensors at that orientation (see solid circles shown in Fig. 4). The time histories of pressure contain high frequency fluctuations, except for the initial impulsive pressures which show clear peaks. To facilitate study of the maximum pressure distributions, the data time interval was reduced from 0.001 s to 0.05 s by applying a moving-maximum window of width 0.05 s and taking the maximum recorded pressure within that window as the pressure value for the time corresponding to the centre of the window. For example, after interval reduction, maximum
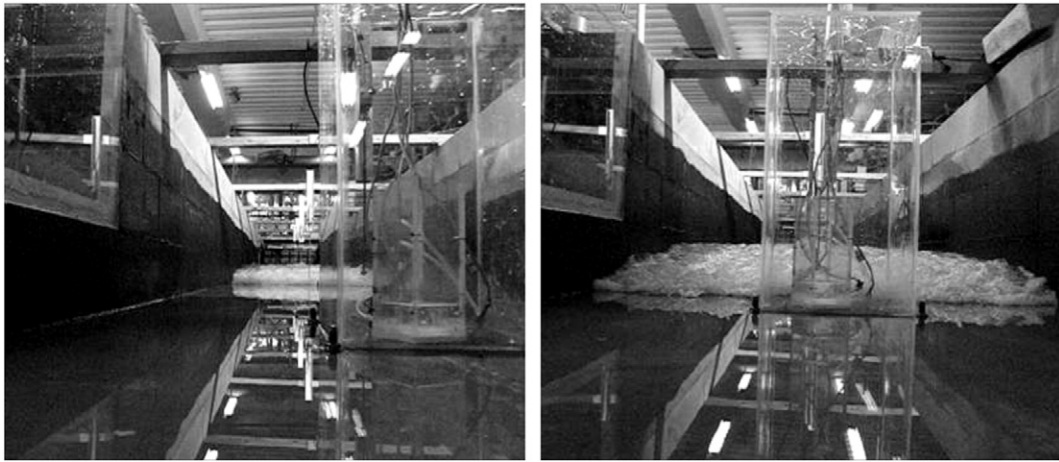

Fig. 7. Relation between average tsunami bore velocity and bore height for different studies, prototype scale.

Fig. 8. An example of the generated bore impinging on the model structure.

instantaneous pressure recorded at $t = 0.2$ s is the maximum value from the original pressure record between $t = 0.175$ s and $t = 0.225$ s. This method of reduction of the amount of data was applied to all the pressure distribution analyses in this study.

Impulsive pressure was observed for structure orientations of 0° and 30°, but not for orientations greater than 30°. For $\theta = 45°$ and $\theta = 60°$, there was a rapid (but not impulsive) rise in pressure at the bottom of the structure from $t = 0.0$ to $t = 0.2$ s, with order of magnitude similar to that of the Sensor 1 quasi-steady pressure; there was a further increase in pressure after 1 s with increase in water depth around the structure. At $\theta = 90°$ and 135°, the instrumented wall was not exposed to the direct impact of the bore, and therefore there was no rise in pressure until water had accumulated around the structure.

Fig. 13 shows vertical distributions of instantaneous maximum pressure over the height of the structure, at $\theta = 0°$ and at different times during the period from $t = 0$ to 3 s. The instantaneous maxima were determined using the moving maximum window.

It can be seen that, at each time shown, all the bore height and velocity cases have similar pressure distributions. Therefore, three representative cases, Case 1 ($h_b = 140$ mm and $u_b = 1.98$ m/s), Case 4 ($h_b = 170$ mm and $u_b = 2.20$ m/s) and Case 6 ($h_b = 210$ mm and $u_b = 2.45$ m/s), were chosen as representative cases to study the evolution of the instantaneous maximum pressure distributions along the structure height for $\theta = 0°$. Hereafter the three representative cases of the bore strength are named 'the weak bore' (Case 1), 'the moderate bore' (Case 4) and 'the strong bore' (Case 6). These three cases cover the range of bore strengths in this study. For these three cases, Fig. 14 illustrates the distribution of normalised instantaneous maximum pressure along the normalised vertical height of the structure, at different times during the period $t = 0$ to 3 s. Elevations along the vertical height of the structure (h_s) are normalised in terms of the specific energy (theoretical maximum water level) at the front of the structure ($h_b + u_b^2 / 2g_n$). The dashed lines show the hydrostatic pressure distribution.

Referring to Fig. 14, water pressure typically increased with depth below the flow surface, as expected. The pressure distributions observed
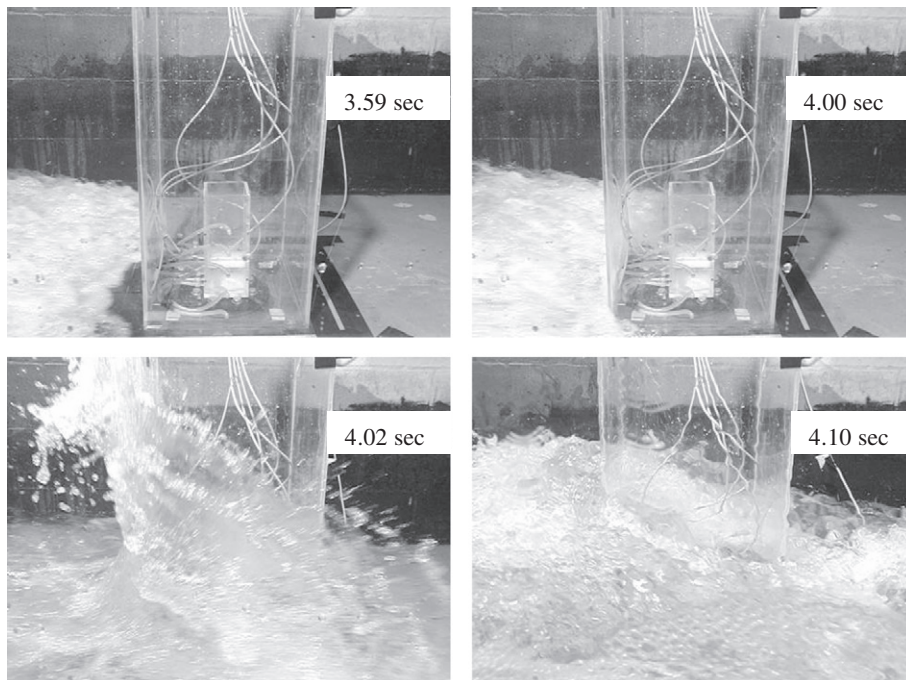

Fig. 9. Photographs taken during experiments for $\theta = 0°$ (i.e. wall perpendicular to the flow); bore travel direction is from left to right.
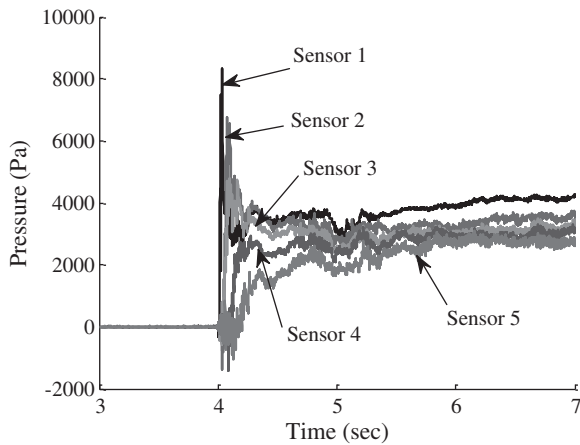
Fig. 10. Average pressure profiles at Sensors 1 through 5 for Case 6.

in this study, for $\theta = 0°$, are similar to those reported by Al-Faesly et al. (2012), Palermo et al. (2012), and Chinnarasri et al. (2013). It is also apparent that the water pressure exceeds hydrostatic pressure. In general the difference is due to the contribution of hydrodynamic pressure. For $t = 0.0$ and 0.2 s, the additional increase is due to impulsive pressure. From Fig. 14, it is obvious that the higher sensors did not initially experience impulsive pressure; these sensors were positioned above the water surface of the toe of the bore. The small values of pressure at the higher sensors at $t = 0$ were probably noise due to vibration of the structure. After initial bore impact, the pressure at the higher sensors increased as the bore height increased around the structure, and the vertical distribution of pressure tended to become linear with a slope similar to that of hydrostatic pressure. The range of pressure magnitudes (for $\theta = 0°$) in this study is similar to those recorded in a study by Al-Faesly et al. (2012) and a study by Palermo et al. (2012). In the studies by Al-Faesly et al. and Palermo et al., the bore velocities were similar to those in this study but the bore heights were 100% larger than in this study, showing the importance of the effect of bore velocity on the pressure.

Fig. 15 shows, for the strong bore, how the vertical pressure distribution varies with orientation and time.

In general, the differences in the distributions of pressure on the structure are due to the deflection of the bore around the structure. At all orientations, the structure experienced positive (i.e. inward) pressure after bore impact, and was never subjected to a negative (i.e. outward) pressure. Overall, increasing the structure orientation to the bore flow decreased the pressure, as expected. During the quasi-steady state the behaviour of the pressure depends on the orientation of the structure. For $\theta = 0°$, there is a wall at right angles to flow,

blocking the water and requiring the flow to turn through 90°. For $\theta = 30°$, 45° and 60°, the corner of the building separates the water much more smoothly, causing a different behaviour in the flow streamlines, and leading to different vertical distributions of pressure. At $\theta = 90°$, the structure experienced almost zero pressure during the first second of bore impact; this is a consequence of flow separation around the structure sides. Accumulation of water around the structure eliminated the separation zone and pressure gradually increased on the structure sides as the depth of water surrounding the structure increased. For $\theta = 135°$, the pressure was zero at all levels for the period of pressure measurement in these experiments, except at $t = 3$ s, when accumulation of water at the rear of the structure caused a small amount of pressure at Sensor 1.

3.3. Tsunami bore induced forces

The multi-axis load cell at the base of the structure was used to measure forces and moments exerted on the structure, for different orientations of the structure to the flow direction (Fig. 3). Fig. 16 shows the time histories of (a) the stream-wise force (F_x) and (b) the vertical (upward) force (F_z), for $\theta = 0°$ and for the three representative cases (i.e. the weak, moderate and strong bores). Measurements were continued until backflow of water disturbed the experiments (about 3 s after initial impact).

For both F_x and F_z, the responses for the three representative experimental cases are similar but have different magnitudes. The magnitudes of the forces increase with increasing bore strength (i.e. bore height and velocity), which is in agreement with results of studies by Santo and Robertson (2010), Al-Faesly et al. (2012) and Palermo et al. (2012). For a 5% larger bore height and a 90% larger bore velocity, Santo and Robertson (2010) measured a 100% larger bore force on a 300 mm wide vertical column; their results are from a large scale experimental set-up in which the bore was generated from a solitary wave breaking on a model beach and with the structure well supported from behind to create a very rigid structure. On the other hand, the range of force values from this study is similar to that from studies by Al-Faesly et al. (2012) and Palermo et al. (2012) for a square prism with the same geometrical size, same bore velocity, but 100% larger bore height. Comparison of our results with the results from previous studies suggests that bore velocity has more effect on the applied force than bore height.

There is an initial rapid rise in the stream-wise force (F_x) as the tsunami bore impacts the structure, reaching a magnitude that is sustained for the duration of the flow past the structure (i.e. until backflow from the end of flume arrives back at the structure). The initial rapid rise in the applied force is due to the initial bore impact which suddenly pushes the structure in the flow direction, but does not exceed the total stream-
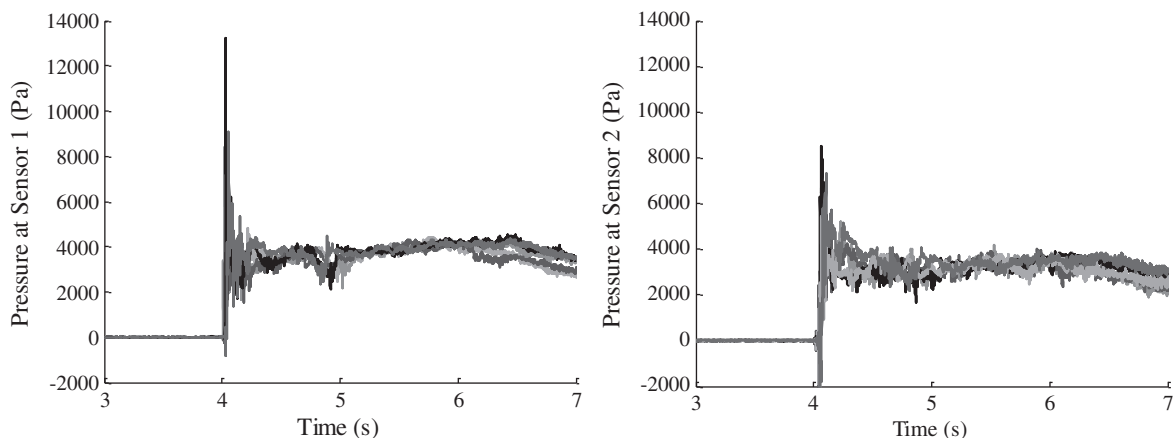

Fig. 11. Time histories of the pressures for Sensors 1 and 2, for five repetitions.
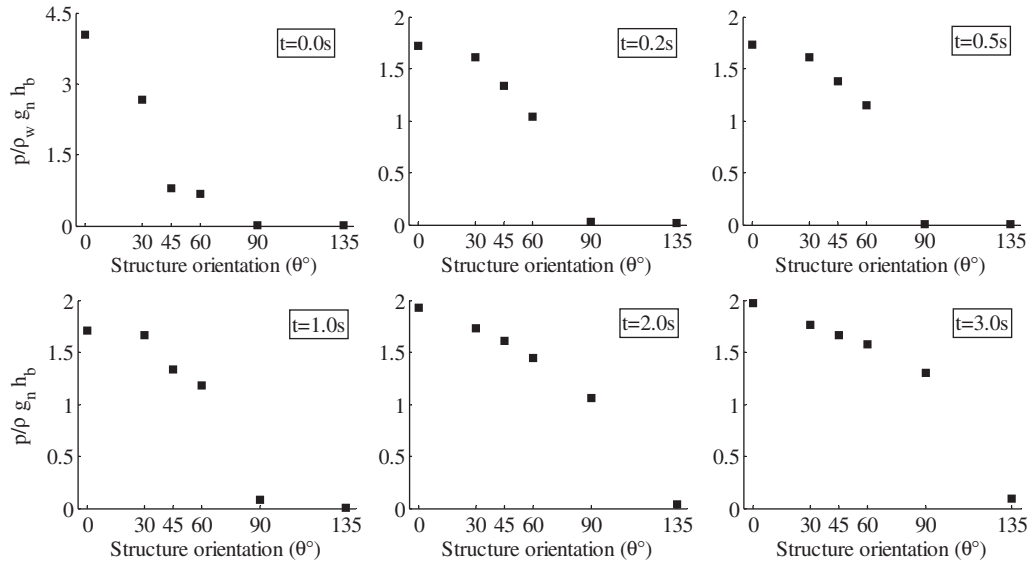
Fig. 12. Pressure variation near the bottom of the structure (Sensor 1) at different structure orientations with respect to the flow direction, for Case 6. Note different pressure range for t = 0.0 s.
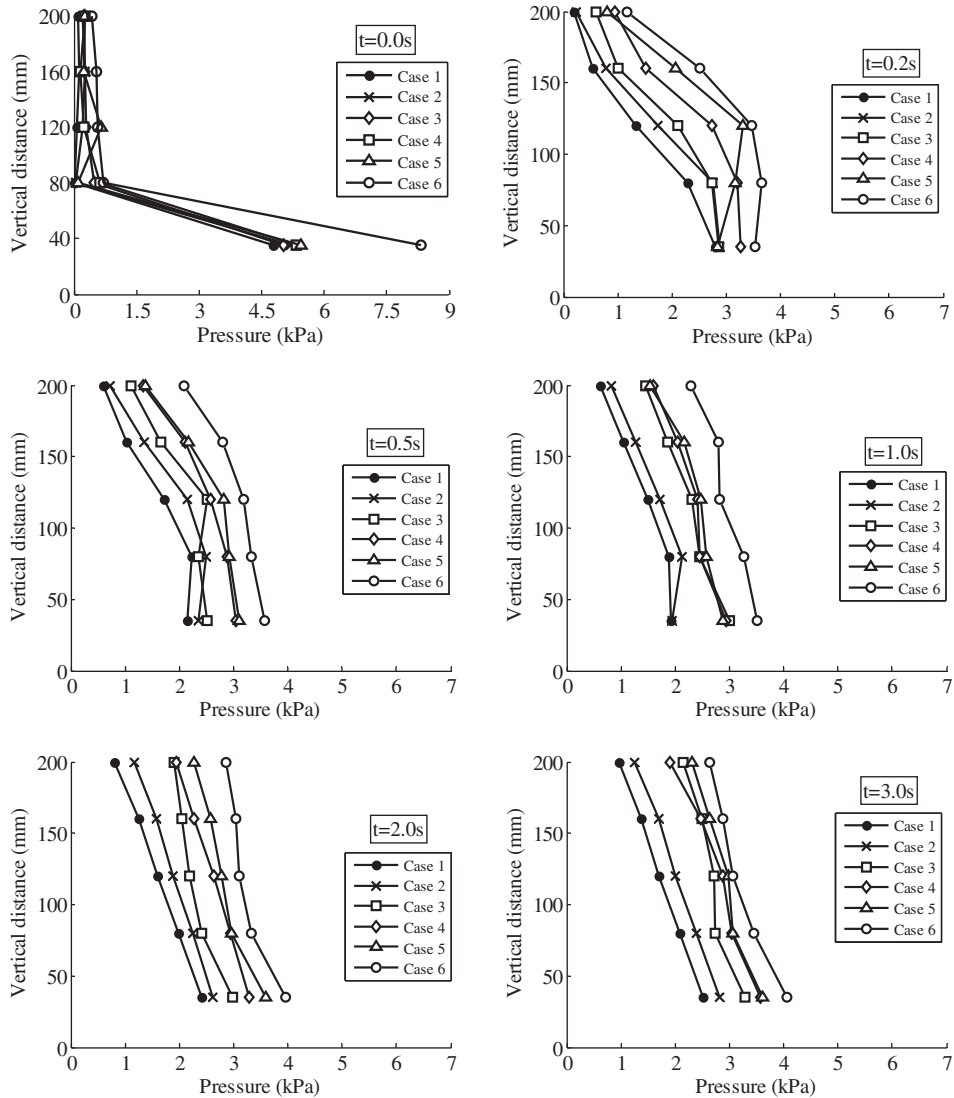

Fig. 13. Vertical distribution of the instantaneous maximum pressure, for $\theta = 0°$, at the time of impact ($t = 0.0$ s) and at various times after impact. All six cases of bore height and velocity are shown.
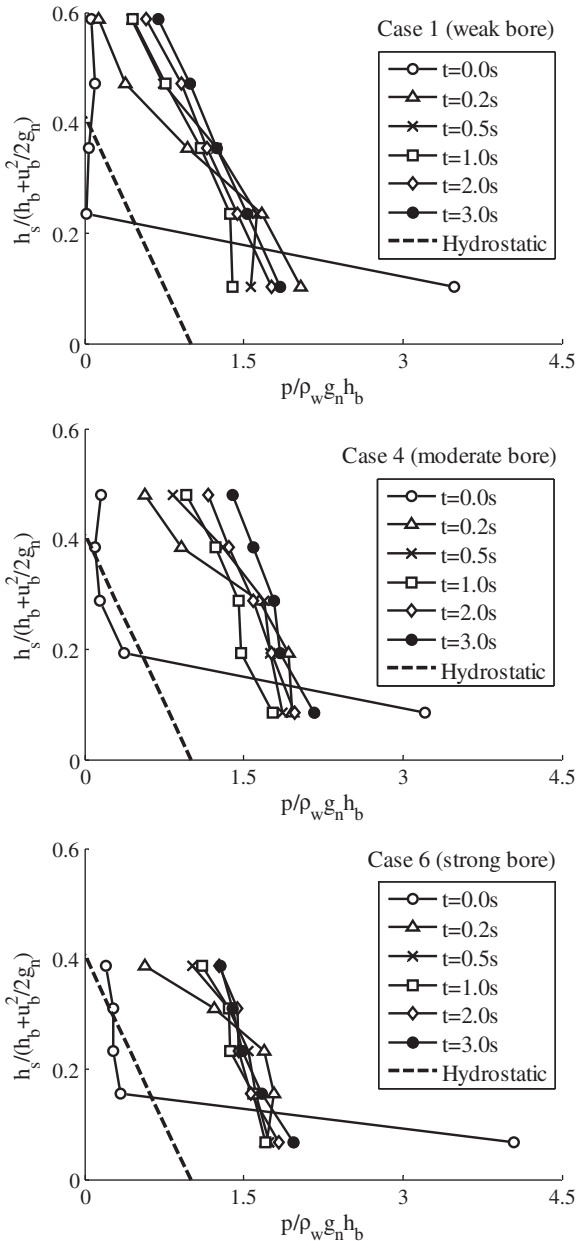
Fig. 14. Vertical distribution of the front wall maximum instantaneous pressure for $\theta = 0°$.

wise force exerted on the structure. This profile of the exerted force is consistent with the profile from investigations by Arnason (2005), and also Nouri et al. (2010) for small bore impacts. However, in contrast to what was observed in this study Nouri et al. (2010) found that the initial bore impact force exceeds the total stream-wise force for larger bores because of their steeper leading fronts. The force while the flow is passing the structure is the resultant of the applied hydrodynamic forces (Nouri et al., 2010).

The vertically upward bore force (F_z) initially increased to approximately the same range of magnitude for all three cases. This initial rise in the upward force is due to flow of the water up the face of the structure height following the initial bore impact. The initial rise was followed by a slower steady approximately linear increase as the depth of water surrounding the structure increased.

Fig. 17 shows, for the strong bore, the temporal variation of F_x for the pairs of orientation $\theta = 0°$ and $90°$, $\theta = 30°$ and $60°$, and $\theta = 45°$ and $135°$.

For each pair, the two time histories are almost the same, as expected. Therefore the three structure orientations of $0°$, $30°$ and $45°$ can

represent the six different orientations to the flow direction investigated in this study. This also illustrates the repeatability of the measured forces in this study.

Variations of force with structure orientation are shown in Fig. 18(a) and 18(b) for F_x and F_z, respectively, for the strong bore. In general, F_x and F_z showed different behaviours under bore impacts.

Fig. 18(a) illustrates that structure orientation has only a small effect on the stream-wise initial bore impact force. The stream-wise initial bore impact force was slightly higher for $\theta = 0°$ than for the other two orientations, and was sustained for a longer duration (15 ms longer in this study). This is because of the different degrees of streamlining of the shapes of the structures. The initial bore impact force decreased with increasing structure orientation, and the minimum initial bore impact force was recorded for $\theta = 45°$. The hydrodynamic force (after the initial impact) was a maximum for $\theta = 30°$. For $\theta = 0°$, the smallest hydrodynamic force was recorded, while the stream-wise initial bore impact force was the largest, as noted above. The changes in the hydrodynamic force with change in θ can be explained by considering the relative effects of the projected area of the structure and the changing effect of streamlining as θ changes. Initially, an increase in the projected area (due to increase in θ, as shown in Fig. 4) dominates, tending to increase the hydrodynamic force. With further increase in θ, the effect of streamlining becomes more significant, leading to a decrease in hydrodynamic force.

Fig. 18(b) shows the variation of F_z for different orientations of the structure. For all orientations, there was an initial quick increase in the upward force, followed by a gradual increase in the force as the depth of water around the structure increased. The maximum upward force was observed for $\theta = 0°$. The F_z time history has a similar shape for $\theta = 0°$ and $30°$, for both of which the structure presents a larger flat face to the flow than for $\theta = 45°$. A short time after bore impact (1.5 s in these experiments), the rate of increase in the upward force for $\theta = 0°$ becomes faster than for the other orientations, because water surrounded the structure faster.

For $\theta = 45°$, after the initial quick rise in the upward force, a quasi-steady state condition is reached for a short period, before the force increases again and follows the same trend as for the other two orientations ($0°$ and $30°$). The more streamlined shape of the structure at $\theta = 45°$ resulted in spatial and temporal variations of the water depth around the structure that were different from those for $\theta = 0°$ and $30°$, and therefore resulted in a different behaviour of the upward force.

3.4. Computation of the forces

Following Cross (1967), it is hypothesised that the tsunami-bore-induced force on the structure is due to the hydrostatic and hydrodynamic forces. The validity of the hypothesis is discussed below.

In general, the water level at the front of the structure is higher than at the rear, with a resulting hydrostatic force given by:

$$F_{hs} = 0.5\rho_w g_n W \left[H^2 - (h_r H)^2 \right] \tag{2}$$

where F_{hs} is the hydrostatic force, ρ_w is the density of water, W is the projected width of the structure to water, H (which exceeds h_b) is the actual water height at the front face of the structure and h_r (which is less than one h_b) is the ratio of the water height at the rear of the structure to the water height in front of the structure. The water level at the rear of the structure was not recorded and had to be estimated from observations and the video records. For $\theta = 0°$, h_r values for the three representative cases, i.e. the weak, moderate and strong bores, were estimated to be 0, 0.12 and 0.20, respectively. The water decelerates when approaching the structure, and the Bernoulli equation can be used to calculate H:
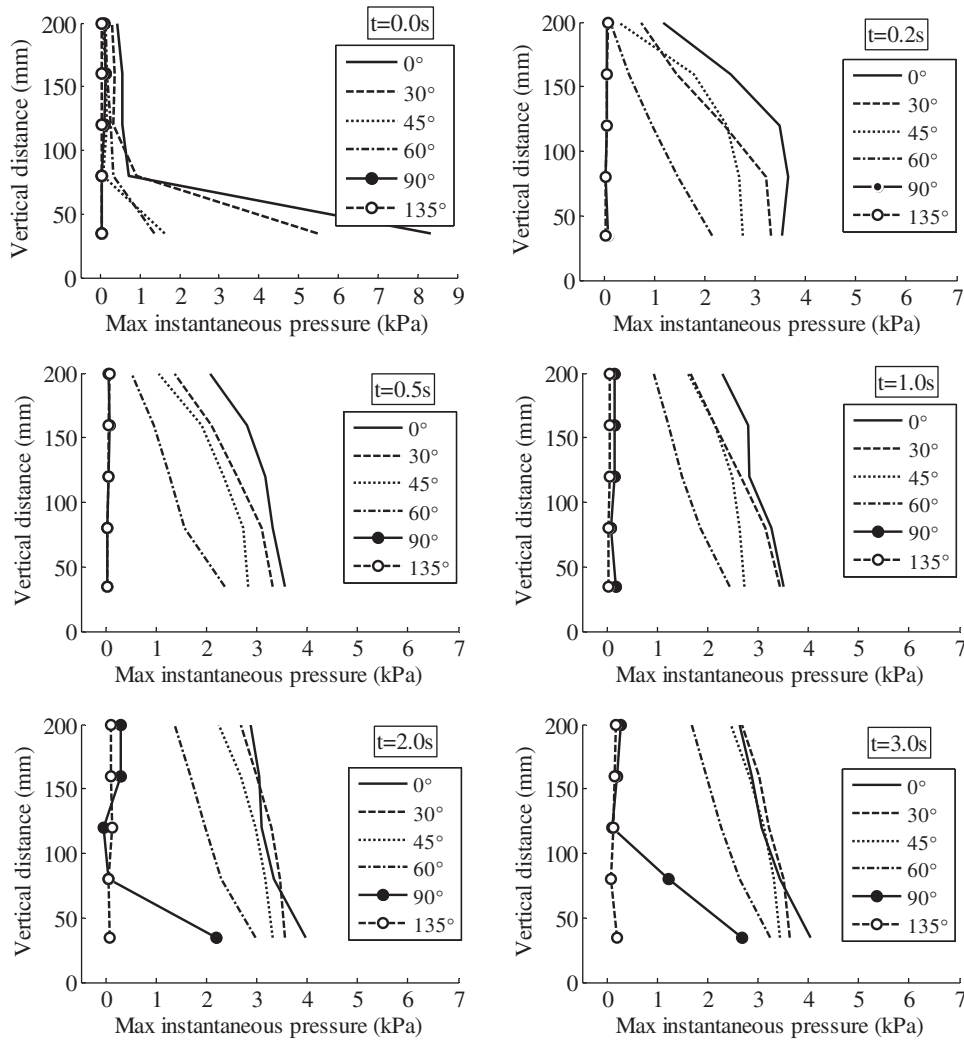
$$H = h_b + c_b \frac{u_b^2}{2g_n} \tag{3}$$

Fig. 15. Evolution of maximum instantaneous pressure at different structure orientations, for strong bore. Note different maximum instantaneous pressure range for $t = 0.0$ s.

in which u_b is obtained from Eq. (1) with $\alpha_u = 1.7$ and, c_b is an empirical coefficient giving the increase in water level (in front of the structure) resulting from a reduction in the bore velocity. The value of c_b depends on the flow velocity and the structure orientation to the flow direction. The actual water height (H) at the front face of the structure was obtained from systematic observation of the video records. Consequently, for $\theta = 0°$, c_b values for the weak, moderate and strong bores were assumed to be 0, 0.14 and 0.20, respectively, where $c_b = 0$ indicates no velocity reduction and, hence, no increase in water depth. The bore height (h_b) was obtained from the penultimate wave gauge. For the
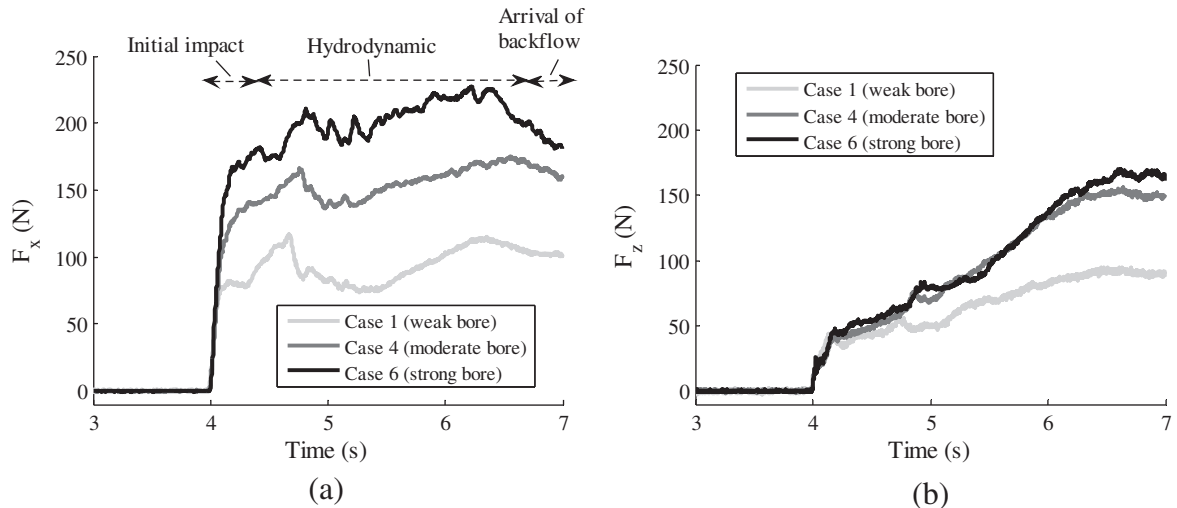

Fig. 16. Time histories of the induced (a) horizontal force (F_x) and (b) vertical force (F_z), with the structure perpendicular to the flow (i.e. $\theta = 0°$).
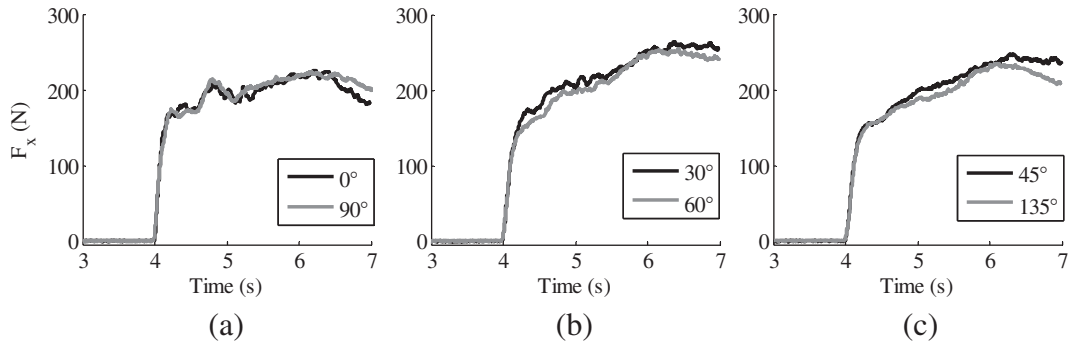
Fig. 17. Time histories of the measured stream-wise force at (a) $\theta = 0°$ and 90°, (b) $\theta = 30°$ and 60° and (c) $\theta = 45°$ and 135°

period of a few seconds after the bore hits the structure the penultimate wave gauge gives a better measure of the bore height (h_b) than the last wave gauge, because the bore height at the last probe is affected by interaction between the bore flow and the structure.

The hydrodynamic force is induced by the quasi-steady flow: it is a function of fluid density, flow velocity and structure geometry, and is given by:

$$F_{hd} = \frac{1}{2}\rho_w C_D W h_b u_b^2 \tag{4}$$

where F_{hd} is the hydrodynamic or drag force due to a tsunami bore, $h_b u_b^2$ is the momentum flux per unit mass per unit width and C_D is the drag coefficient. The $h_b u_b^2$ term is calculated using Eq. (5).

$$h_b u_b^2 = \left(\frac{1 + h_r}{2}H\right)u_b^2 \tag{5}$$

where h_r and H are defined above for Eq. (2). In Eq. (5), the term in parenthesis indicates the average water level surrounding the structure. For a steady flow past a square rod, perpendicular to the flow and with Reynolds number $> 10^4$, Potter et al. (2011) give $C_D = 2.0$. According to FEMA (2000), the value of drag coefficients for square prisms at $\theta = 0°$ and for free-surface flows varies from 1.2 to 2.0 depending on the width to height ratio. The laboratory experiments by Arnason (2005) indicated a $C_D = 2.0$ for a square prism at $\theta = 0°$, which is also adopted by FEMA (2012). Yeh (2006) noted that available C_D values (for particular shapes and Reynolds numbers) apply to steady flows, while tsunamis are not steady. Considering a long tsunami period and quasi-steady conditions, Eq. (4) is applicable to tsunami bore force if an appropriate C_D is chosen. To find an appropriate C_D value for this study, the hydrodynamic force component was calculated by

subtracting the hydrostatic force component (calculated from Eq. (2)) from the total force measured by the load cell. Application of Eq. (4) to this calculated hydrodynamic force gave a C_D value of 1.65.

The total stream-wise force (F_{ht}) can be obtained from the summation of the hydrostatic and hydrodynamic forces (Cross, 1967) as:

$$F_{ht} = F_{hs} + F_{hd}. \tag{6}$$

Fig. 19 illustrates, for the strong bore and $\theta = 0°$, the average measured force (average from five repetitions), calculated force from integration of the measured pressure, hydrostatic force (Eq. (2)), and hydrodynamic force (Eq. (4)).

The pressure integration method was that used by Thusyanthan and Madabhushi (2008) and Robertson et al. (2013). The surface was divided horizontally into strips on which the pressure is assumed to be constant. The boundaries between the calculation strips are taken as midway between adjacent sensors (Tiessen Polygons method). The main advantage of recording the pressure as well as the force is that it allows calculation of the spatial variation of force up the face of the structure. Fig. 19 shows that integration of pressure successfully reproduced the total force measured by the load cell, showing the validity of the force and pressure measurement techniques used in this study.

For the period from 0.0 to 0.5 s after bore impact, the initial rise in the measured force has a steeper slope than that of the force calculated from Eq. (6). The difference in the initial rise is a consequence of the bore height profile measured by the wave gauge which is more gradual than that of the measured force. For the period from 0.5 to 2.0 s after bore impact the total stream-wise force was computed with an acceptable range of variation.

Eq. (6) was also used to compute the bore induced force on the structure for $\theta = 30°$ and 45°. The method used for obtaining the drag

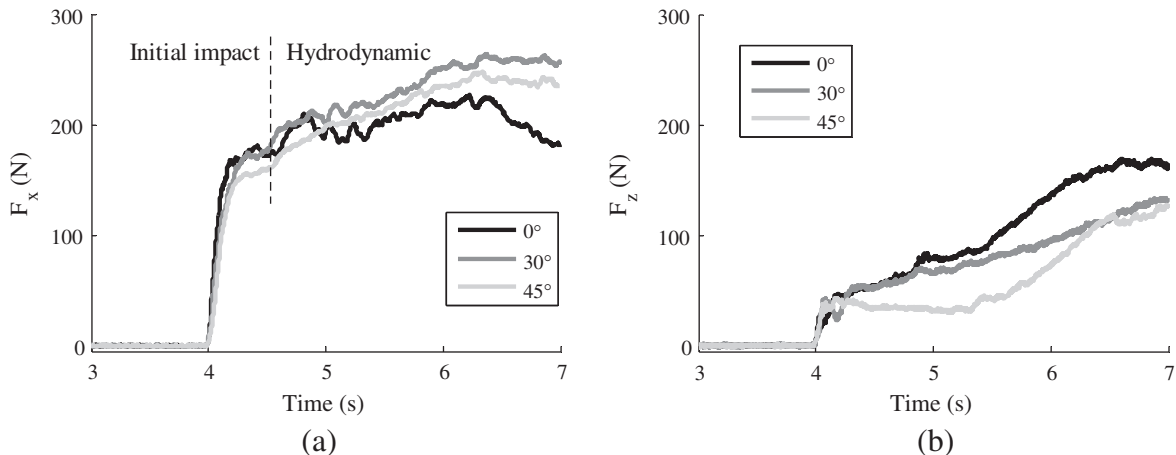**Fig. 18.** Time histories of the applied (a) F_x and (b) F_z on the structure at different orientations to the flow direction, for the strong bore.

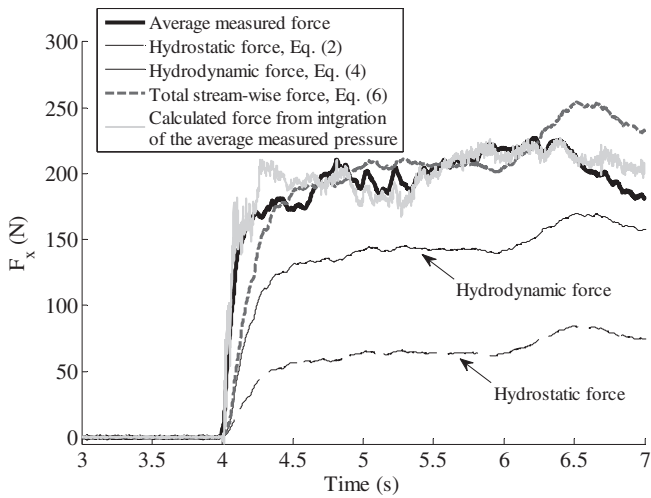**Fig. 19.** Comparison of the time histories of the measure bore force, for the strong bore and $\theta = 0°$, with forces computed from Eq. (6) and the measured pressure integration.

coefficients for the structure at $\theta = 30°$ and $45°$ was the same as that used for the structure at of $\theta = 0°$. The hydrodynamic forces were calculated by subtracting the hydrostatic forces from the total measured forces from the load cell. These hydrodynamic forces resulted in $C_D = 1.4$ and 1.15 for $\theta = 30°$ and $45°$, respectively. For a steady flow past a square rod, at $45°$ to the flow and with Reynolds number $>10^4$, Potter et al. (2011) give a C_D value of 1.6.

Figs. 20(a) and 20(b) show the average measured force, total stream-wise force computed using Eq. (6), and force calculated from integration of the measured pressure, for the strong bore, and for $\theta = 30°$ and $45°$, respectively.

Figs. 20(a) and 20(b) indicate that there is good agreement between the measured forces and the computed forces. Therefore, Eq. (6) can be used to obtain estimates of the forces due to a tsunami bore, for a structure with square plan shape, for different structure orientations using appropriate drag coefficients.

Several studies have suggested estimating the initial impact force of a tsunami bore by adaptation of the hydrostatic equation. For example, Fujima et al. (2009) suggest:

$$F_{su} = \alpha \rho_w g_n W h_b^2 \tag{7}$$

where F_{su} is the initial impact force of a tsunami, and α is the hydrostatic force coefficient. For the results of this study, the equivalent values of α ranged from 2.7 to 3.5 for the measured forces resulting from different bore strengths. Previous studies suggest that values of α are in the range 4.5 to 6 (Asakura et al., 2000; Fujima et al., 2009; Thusyanthan and Madabhushi, 2008). Comparison of the results from this study with those from previous studies illustrates the difficulty of determining a uniform method for estimating tsunami bore forces on structures.

For the hydrodynamic force estimation, FEMA (2011) recommend using Eq. (4), with $C_D = 2.0$ for rectangular structures. In this study, C_D values varied from 1.15 to 1.65 for the maximum hydrodynamic force recorded after bore impact. This suggests that previous studies overestimated the hydrodynamic force by using drag coefficients that were too high. Moreover, FEMA (2012) suggested consideration of a brief impulsive phase of the bore force at the initial time of impact, equivalent to 1.5 times the hydrodynamic force. In this study, the bore front had a gentle sloping front ($<15°$) and hence the impulsive force was not present for the cases of bore impact investigated (see also Cross (1967)).

A hydrodynamic uplift force occurs in combination with a buoyant force. A hydrodynamic uplift force is exerted on the structure because of the vertical velocity component of the rapidly rising water as the bore impacts the structure. However in this experiment, only the buoyancy force (F_{bu}) was considered, as below.

$$F_{bu} = \rho_w g_n \left(\frac{1 + h_r}{2} H \right) A_s \tag{8}$$

where A_s is the area of the structure base. It was assumed that, after initial impact of the bore, no further water rise occurred in front of the structure. Even if this may not be completely true, it was considered that a rise at the front will be compensated for by a rise of water level at the rear. If the water can flow more easily around the structure, the level in the front will be less, but more water will be able to accumulate at the back. The same h_r values estimated for the stream-wise force were used in calculation of the upward force. As an example, Fig. 21 shows the computed upward force (using Eq. (8)) and the average measured upward force from the load cell (average from five repetitions), for the strong bore and $\theta = 0°$.

Both the trend and the magnitude of the upward force are estimated well by Eq. (8), showing that the assumed c_b values are validated. Differences are probably caused by fluctuations in the wave gauge water level record, which cannot be avoided in these experiments. It can therefore be assumed that the use of Eq. (8) is acceptable. In addition, Fig. 21
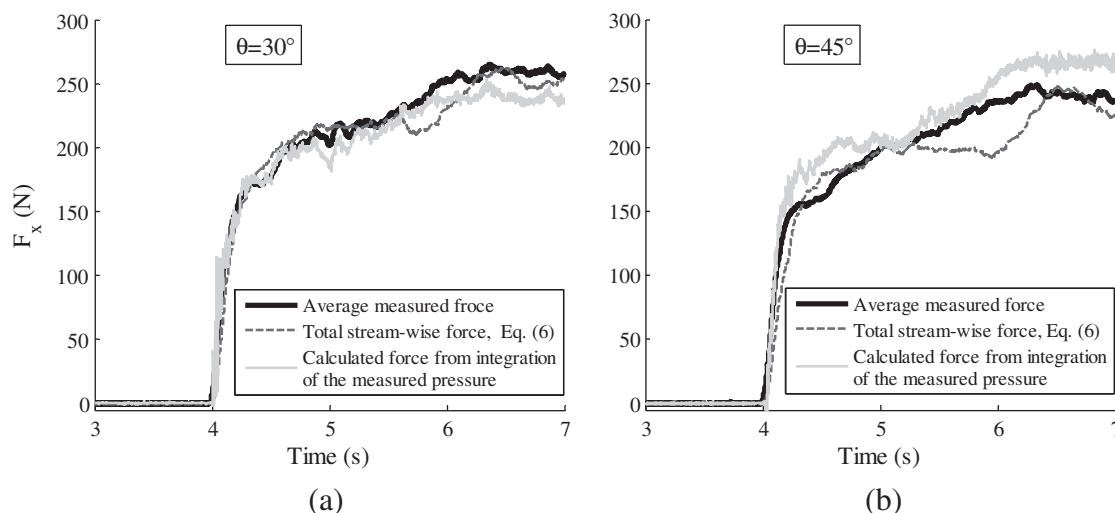

Fig. 20. Computation of the bore force for (a) $\theta = 30°$ and (b) $\theta = 45°$.
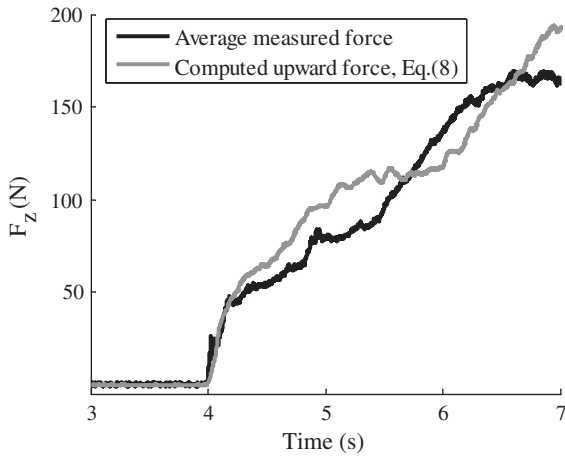
Fig. 21. Time histories of the measured and the computed upward forces.

indicates that, for the tsunami bore in this study, the hydrodynamic up-lift force is negligible.

3.5. Tsunami bore induced moments

The measured overturning moment (M_y) and twisting moment (M_z) are given in Fig. 22(a) and 22(b), respectively, for the three representative cases (i.e. the weak, moderate and strong bores) and $\theta = 0°$.

The variations in the overturning moment with time after impact and with bore height and velocity are similar to those for the applied force, as expected (see Fig. 16(a)). The twisting moments were small. The flow was symmetrically distributed around the structure, resulting in similar forces on both sides of the vertical plane of symmetry of the structure. The relationship between the overturning moments and stream-wise bore forces is shown in Fig. 23, for the three representative cases (i.e. the weak, moderate and strong bores) and $\theta = 0°$.

In general, increasing force leads to increasing overturning moment. In addition, for low values of force, i.e. $F_x < 80$ N, the relationship between force and moment is independent of h_b and u_b. However, with increasing applied force, it is apparent that the force–moment relationship becomes dependent on h_b and u_b. For each representative case, there was a bi-linear relationship between force and moment, with hinge point at F_x values of about 78, 112 and 140 N for the weak, moderate and strong bores, respectively. This bi-linear relationship can be referred to the temporal variation of the centre of effort of the

resultant stream-wise force on the front wall of the structure. The slope of each line in Fig. 23 gives the height of the centre of effort of the stream-wise force. For the three representative cases (i.e. the weak, moderate and strong bores) and $\theta = 0°$, the time history of the height of the centre of effort of the stream-wise force (normalised by the bore height), was calculated by dividing the measured moments by the measured forces, as shown in Fig. 24.

In general, the height of the centre of effort of the maximum induced force was proportional to the bore height (i.e. normalised height $= 1.0$). However, the ratio of the centre of effort to the bore height was larger for the weak and moderate bores than for the strong bore. Because of the significant obstruction of the flow by the structure at $\theta = 0°$, the water level in front of the structure (after the initial bore impact) increased significantly. Hence, the centre of effort of the force on the structure suddenly shifted to a level above the equivalent bore height level.

4. Conclusions

The following conclusions are drawn from the experimental work presented herein.

1. The bore velocity u_b is equal to about $1.7(g_n h_b)^{0.5}$ where h_b is the bore height. The coefficient value of 1.7 is within 7% and 10% of the values proposed by Murty (1977) and FEMA (2012), respectively.
2. For $\theta = 0°$ and the quasi-steady state, where the hydrodynamic pressure is dominant, the pressure distributions tended to have a slope similar to that of the hydrostatic pressure.
3. The pressure distribution depends on the orientation of the structure with respect to flow direction. At all orientations, the bore flow always exerted a positive (i.e. inward) pressure on the structure, and negative (i.e. outward) pressure was not observed. Overall, increasing the structure orientation to the bore flow decreased the pressure.
4. Bore velocity seems to have a larger effect on tsunami bore pressure than bore height.
5. For bores with fronts sloping at less than 15°, the maximum bore force on the structure can be estimated for design purposes the sum of hydrostatic and hydrodynamic forces.
6. The hydrostatic force should be calculated as a resultant force from the actual water level at the front face of the structure and water level at the rear of the structure. Eq. (2) gives an acceptable estimation of the hydrostatic force, providing an appropriate bore velocity reduction factor, i.e. c_b in Eq. (3), is chosen.
7. The drag coefficient is a function of the structure orientation with respect to the flow direction; results gave C_D values of 1.65 for $\theta = 0°$. The C_D value decreased as θ increased, with values of 1.4 and 1.15 at
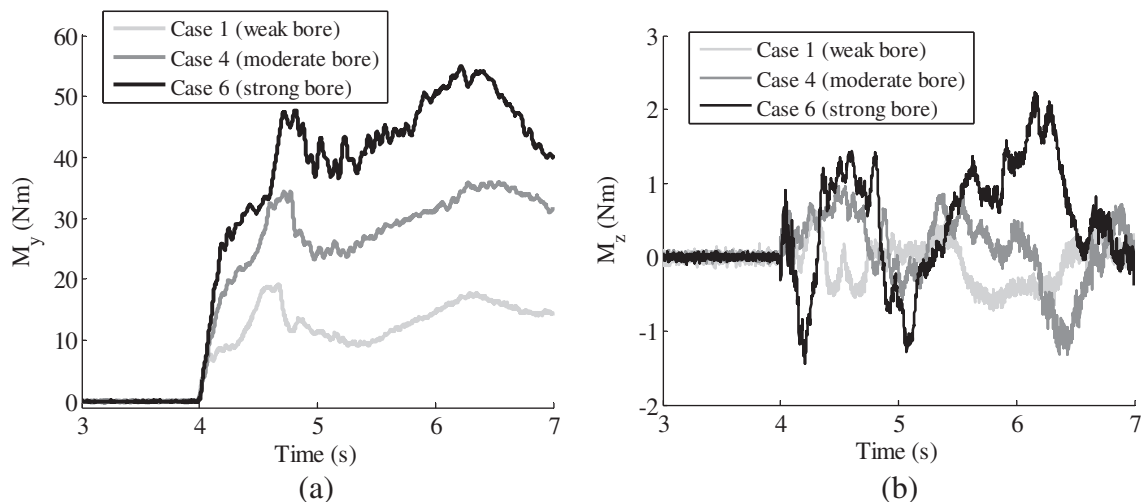

(a)

(b)

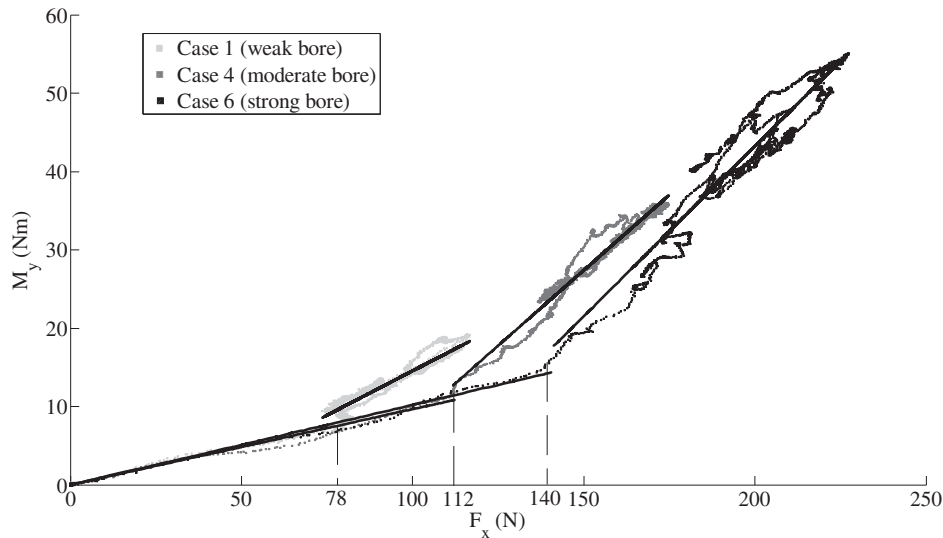Fig. 22. Time histories of (a) overturning moment and (b) twisting moment, at $\theta = 0°$.

Fig. 23. Relationship between applied force and overturning moment, at $\theta = 0°$; thresholds of changes in the relationship are emphasised by adding the trend lines. For a bi-linear relationship, the hinge point is where the two lines interact.

$\theta = 30°$ and $\theta = 45°$, respectively. These values give preliminary guidance for design.

8. For bores with fronts sloping at less than 15°, the upward force is due to buoyancy, and the hydrodynamic uplift force is negligible. Eq. (8) gives a reasonable estimation of the design upward force.

9. The measured pressures were integrated to obtain the time history of stream-wise force, assuming uniform pressure distribution over the width of the structure. The resulted time history of the force has similar shape and magnitude to that measured from the load cell, validating the methodology of this study.

Further investigation would facilitate refinement of the relationship between c_b and bore characteristics for a given structure geometry.
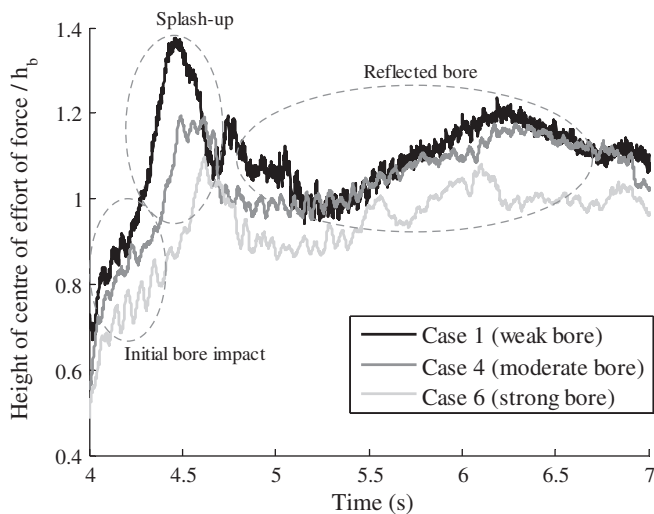
Acknowledgements

Fig. 24. Time history of the normalised height of the centre of effort of the stream-wise force, for $\theta = 0°$.

References

Al-Faesly, T., Palermo, D., Nistor, I., Cornett, A., 2012. Experimental modeling of extreme hydrodynamic forces on structural models. Int. J. Prot. Struct. 3 (4), 477–506.

Arnason, H., 2005. Interactions between an incident bore and a free-standing coastal structure. University of Washington, Washington, USA 172 pp.

Asakura, R., et al., 2000. An experiment study on wave force acting on on-shore structures due to overflowing tsunamis. Proc. Coast. Eng. 911–915 (JSCE).

Bryant, E., 2001. Tsunami: The Underrated Hazard. Cambridge University Press (320 pp.).

Bullock, G., Obhrai, C., Peregrine, D., Bredmose, H., 2007. Violent breaking wave impacts. Part 1: results from large-scale regular wave tests on vertical and sloping walls. Coast. Eng. 54 (8), 602–617.

Cawley, J.G., 2014. Review of Guidelines for the Design of Tsunami Vertical Evacuation Buildings. Oregon State University (92 pp.).

CCH, 2000. City and County of Honolulu Building Code (Chapter 16, Article 11) Department of Planning and Permitting, Honolulu, Hawaii.

Chanson, H., 2006. Tsunami surges on dry coastal plains: application of dam break wave equations. Coast. Eng. J. 48 (4), 355–370.

Chinnarasri, C., Thanasisathit, N., Ruangrassamee, A., Weesakul, S., Lukkunaprasit, P., 2013. The impact of tsunami-induced bores on buildings. Proc. ICE-Marit. Eng. 14–24.

Cooker, M.J., Peregrine, D., 1995. Pressure-impulse theory for liquid impact problems. J. Fluid Mech. 297, 193–214.

Cross, R.H., 1967. Tsunami surge forces. J. Waterw. Harb. Div. ASCE 93 (4), 201–231.

Dias, P., Dissanayake, R., Chandratilake, R., 2006. Lessons Learned from Tsunami Damage in Sri Lanka. pp. 74–81.

FEMA, 2000. Coastal Construction Manual. Federal Emergency Management Agency, Washington D.C., USA (USA).

FEMA, 2011. Coastal Construction Manual: Principles and Practices of Planning, Siting, Designing, Constructing, and Maintaining Residential Buildings in Coastal Areas. fourth ed. Federal Emergency Management Agency (FEMA P-55).

FEMA, 2012. Guidelines for Design of Structures for Vertical Evacuation from Tsunamis (FEMA P646). Federal Emergency Management Agency, Washington, USA (http://www.fema.gov/media-library-data/1426211456953-f02dffee4679d659f62f414639afa806/FEMAP-646_508.pdf (access 14/06/2015)).

Foytong, P., Ruangrassamee, A., Shoji, G., Hiraki, Y., Ezura, Y., 2013. Analysis of tsunami flow velocities during the March 2011 Tohoku, Japan, tsunami. Earthquake Spectra 29 (s1), S161–S181.

Fraser, S., Leonard, G., Matsuo, I., Murakami, H., 2012. Tsunami Evacuation: Lessons from the Great East Japan Earthquake and Tsunami of March 11th, 2011. GNS Science.

Fritz, H., Synolakis, C., McAdoo, B., 2006. Maldives field survey of the 2004 indian ocean tsunami, 2004 great Sumatra earthquakes and indian ocean tsunamis of December 26, 2004 and March 28, 2005. Earthquake Spectra 22.

Fritz, H.M., et al., 2012. The 2011 Japan tsunami current velocity measurements from survivor videos at Kesennuma bay using lidar. Geophys. Res. Lett. 39 (7), L00G23.

Fujima, K., Achmad, F., Shigihara, Y., Mizutani, N., 2009. Estimation of tsunami force acting on rectangular structures. J. Disaster Res. 4 (6), 404–409.

Ghobarah, A., Saatcioglu, M., Nistor, I., 2006. The impact of the 26 december 2004 earthquake and tsunami on structures and infrastructure. Eng. Struct. 28 (2), 312–326.

Hattori, M., Arami, A., Yui, T., 1994. Wave impact pressure on vertical walls under breaking waves of various types. Coast. Eng. 22 (1-2), 79–114.

Hayashi, S., Koshimura, S., 2013. The 2011 Tohoku tsunami flow velocity estimation by the aerial video analysis and numerical modeling. J. Disaster Res. 8 (4), 561–572.

Hibberd, S., Peregrine, D.H., 1979. Surf and run-up on a beach: a uniform bore. J. Fluid Mech. 95 (2), 323–345.

Iizuka, H., Matsutom, H., 2000. Damage due to flooding flow of tsunami. Proceedings of Coastal Engineering, Japan Society of Civil Engineers, pp. 381–385.

Jaffe, B.E., et al., 2012. Flow speed estimated by inverse modeling of sandy tsunami de-
posits: results from the 11 March 2011 tsunami on the coastal plain near the Sendai
Airport, Honshu, Japan. Sediment. Geol. 282, 90–109.
Kihara, N., et al., 2015. Large-scale experiments on tsunami-induced pressure on a vertical
tide wall. Coast. Eng. 99, 46–63.
Kirkoz, M., 1983. Breaking and run-up of long waves, tsunamis: their science and engi-
neering. Proceedings of the 10th IUGG International Tsunami Symposium.
Lauber, G., Hager, W.H., 1998. Experiments to dambreak wave: Horizontal channel.
J. Hydraul. Res. 36 (3), 291–307.
Linton, D., et al., 2013. Evaluation of tsunami loads on wood-frame walls at full scale.
J. Struct. Eng. 139 (8), 1318–1325.
Liu, H., et al., 2013. The 11 March 2011 Tohoku tsunami survey in Rikuzentakata and com-
parison with historical events. Pure Appl. Geophys. 170 (6-8), 1033–1046.
Lloyd, T., Rossetto, T., 2012. A comparison between existing tsunami load guidance and
large-scale experiments with long-waves. 15 World Conference on Earthquake
Engineering.
Matsutomi, H., Okamoto, K., 2010. Inundation flow velocity of tsunami on land. Island Arc
19 (3), 443–457.
Matsutomi, H., Sakakiyama, T., Nugroho, S., Matsuyama, M., 2006. Aspects of inundated
flow due to the 2004 indian ocean tsunami. Coast. Eng. J. 48 (2), 167–195.
Mizutani, S., Imamura, F., 2001. Dynamic wave force of tsunamis acting on a structure. ITS
2001 Proceedings, pp. 941–948.
Murty, T.S., 1977. Seismic Sea Waves: Tsunamis. Dept. of Fisheries and the Environment,
Fisheries and Marine Service, Ottawa.
Nistor, I., Palermo, D., Cornett, A., Al-Faesly, T., 2011. Experimental and numerical model-
ing of tsunami loading on structures. Coastal Engineering Proceedings, pp. 1–14.
Nouri, Y., 2008. The impact of hydraulic bores and debris on free standing structures.
MR50910 Thesis. University of Ottawa (Canada), Canada (139 pp.).
Nouri, Y., Nistor, I., Palermo, D., 2010. Experimental investigation of tsunami impact on
free standing structures. Coast. Eng. J. 52 (1), 43–70.
Okamura, M., 1993. Impulsive pressure due to wave impact on an inclined plane wall.
Fluid Dyn. Res. 12 (4), 215–228.
Palermo, D., Nistor, I., Al-Faesly, T., Cornett, A., 2012. Impact of tsunami forces on struc-
tures: the University of Ottawa experience. 5th International Tsunami Symposium,
pp.
Palermo, D., Nistor, I., Nouri, Y., Cornett, A., 2009. Tsunami loading of near-shoreline struc-
tures: a primer. Can. J. Civ. Eng. 36 (11), 1804–1815.
Peregrine, D., 2003. Water-wave impact on walls. Annu. Rev. Fluid Mech. 35 (1), 23–43.
Potter, M., Wiggert, D., Ramadan, B., 2011. Mechanics of Fluids SI Version. Cengage
Learning.
Rahman, S., Akib, S., Khan, M., Shirazi, S., 2014. Experimental study on tsunami risk reduc-
tion on coastal building fronted by sea wall. Sci. World J. 2014, 7.

Ramsden, J.D., 1993. Tsunamis: Forces on a Vertical Wall Caused by long Waves, Bores,
and Surges on a Dry Bed. California Institute of Technology, California, United States
(278 pp.).
Ritter, A., 1892. The propagation of water waves. Ver. Dtsch. Ing. Z. 36 (33 part 3),
947–954.
Robertson, I., Paczkowski, K., Riggs, H., Mohamed, A., 2011. Tsunami bore forces on walls.
30th International Conference on Ocean, Offshore and Arctic Engineering,
pp. 395–403.
Robertson, I., Riggs, H., Mohamed, A., 2008. Experimental results of tsunami bore forces
on structures. Proceedings of the 27th International Conference on Offshore Mechan-
ics and Arctic Engineering, pp. 15–20.
Robertson, I.N., Carden, L.P., Chock, G.Y., 2013. Case study of tsunami bore impact on
rc wall. 32nd International Conference on Ocean, Offshore and Arctic Engineer-
ing (pp. V005T06A077-V005T06A077).
Rossetto, T., et al., 2007. The Indian Ocean tsunami of December 26, 2004: observations in
Sri Lanka and Thailand. Nat. Hazards 42 (1), 105–124.
Saatcioglu, M., Ghobarah, A., Nistor, I., 2006. Effects of the December 26, 2004 Sumatra
earthquake and tsunami on physical infrastructure. ISET J. Earthq. Eng. Technol. 42
(4), 79–94.
Santo, J., Robertson, I.N., 2010. Lateral Loading on Vertical Structural Elements due to a
Tsunami Bore. University of Hawaii, Honolulu.
Shimozono, T., et al., 2012. Propagation and inundation characteristics of the 2011 Tohoku
tsunami on the central Sanriku coast. Coast. Eng. J. 54 (1), 1250004-1–1250004-17.
Suppasri, A., et al., 2012. Damage charachteristic and field survey of the 2011 great east
Japan tsunami in Miyagi prefecture. Coast. Eng. J. 54 (1), 1250005-1–1250005-30.
Thusyanthan, N., Madabhushi, G.S., 2008. Tsunami wave loading on coastal houses: a
model approach. Civ. Eng. 161 (2), 77–86.
Tomita, T., Imamura, F., Arikawa, T., Yasuda, T., Kawata, Y., 2006. Damage caused by the
2004 Indian Ocean tsunami on the southwestern coast of sri lanka. Coast. Eng. J. 48
(2), 99–116.
Wijatmiko, I., Murakami, K., 2012. Study on the Interaction Between Tsunami Bore and
Cylindrical Structure with Weir. INTECH Open Access Publisher, pp. 59–78.
Yeh, H., 2006. Maximum fluid forces in the tsunami runup zone. J. Waterw. Port Coast.
Ocean Eng. 132 (6), 496–500.
Yeh, H., 2007. Design tsunami forces for onshore structures. J. Disaster Res. 2 (6),
531–536.
Yeh, H., Sato, S., Tajima, Y., 2013. The 11 March 2011 east Japan earthquake and tsu-
nami: tsunami effects on coastal infrastructure and buildings. Pure Appl.
Geophys. 170 (6-8), 1019–1031.
Yeh, H.H., 1991. Tsunami bore runup. Nat. Hazards 4 (2), 209–220.